

# Semi-Deterministic and Stochastic Sampling of Feynman Diagrams with $1/N_f$ Expansions

Boyuan Shi<sup>1,\*</sup>

<sup>1</sup>*Blackett Laboratory, Imperial College London, London SW7 2AZ, United Kingdom*

We introduce a family of (semi) bold-line series, assisted with  $1/N_f$  expansions, with  $N_f$  being the number of fermion flavours. If there is no additional  $N_f$  cut, the series reduces to the RPA series in the density-density channel, complementary to the particle-hole and particle-particle channels introduced in [Phys. Rev. B **102**, 195122]. We performed extensive benchmarks for density, energy and pressure with  $t-t'$   $SU(N_f)$  Hubbard model on square lattice and honeycomb lattices over a wide range of numerical methods. For benchmark purposes, we also implement bare-U symmetry-broken perturbation series for the 2D  $SU(2)$  Hubbard model on the honeycomb lattice. We find difficulties simulating grand potentials with different shift parameters even at high temperatures and weak interactions, while in general find encouraging results for density simulations. We believe the search for optimal shift parameters is feasible, while we leave this problem for future studies. Nevertheless, the  $1/N_f$  series could prove efficacious for grand potential computations where symmetry broken bare-U expansion grapples with considerable challenges.

## I. INTRODUCTION

Accurately simulating quantum many-body systems to understand and predict materials properties has high academic and industrial values. The major bottleneck for real material simulations is the exponential wall problem for large systems. Finite-size effects are critical in many aspects of material simulations, as they can significantly influence the accuracy of results. In particular, small scale simulations may not fully capture long-range correlations. At the vicinity of phase transitions, divergence of correlation length makes it difficult to extrapolate to the thermodynamic limit. The other issue is the inclusion of multiple orbitals and interaction matrix elements. Properly handling them is already challenging for methods that only require limited computational resources, such as GW and its extensions [1].

Field theoretical approaches among concurrent methods [1–10] usually could be applied to sufficiently large systems. Unless at extremely low temperatures or ground state for some special cases, real materials simulations are typically free from both the UV and IR divergence, and perturbation series based on interaction strength could acquire a finite radius of convergence. The very primordial idea to push it to higher orders stages a comeback with the advent of computing power, with numerous studies showing its unprecedented accuracy over many models that are close to real materials.

With the finite-size effects seemingly resolved by this class of methods, the simple change of model from one-band to two-bands considerably circumscribes the applicability of a wide range of highly accurate numerical methods due to the additional exponential growth of computational costs. In particular, although the family of diagrammatic Monte Carlo (DiagMC) methods have superior accuracy over other field theoretical methods, it suffers from such problems.

For methods within the DiagMC family, computational costs for complicated lattice geometries and more interaction matrix elements increase exponentially with the state-of-arts principal minor algorithms. The very recent GPU speed-up based on adaptations of a combinatorial algorithm for determinants [11] provides a promising routine but algorithmic adaptations for different lattice and interaction configurations are highly nontrivial.

The other major problem of diagrammatic Monte Carlo is the enlargement of its radius of convergence and the reliability of re-summation. The region of analyticity of any power series is delineated by a circle. For example, even if there is no phase transition in weakly-interacting fermi liquids, the negative interaction value on the other side might well correspond to a superfluid phase transition or BCS instability. Therefore, re-summation must be invoked at almost all the times. That does not appear to constitute a significant impediment given that sufficiently high orders of the perturbation series can be reached. Indeed, this has been extensively examined in 2D and 3D Hubbard models on square and cubic lattices. However, two underlying assumptions must be invoked. That the maximum truncation order around nine to ten is generally sufficient and the analytical structure remains sufficiently accommodating for the functionality to persist when generalizing to real materials.

---

\* [boyuanshi0607@gmail.com](mailto:boyuanshi0607@gmail.com)

The breakdown of these assertions may plausibly manifest in previously studied models, yet remain undisclosed. Nevertheless, we attempted the Hubbard model on the honeycomb lattice using the state-of-art symmetry broken perturbation series and reported issues of the method for grand-potential computations. Interestingly, for identical set of parameters where grand potential deviates from the true value significantly, density could match with the exact results to four decimal places. Indeed, the pursuit of optimal shift parameters can be refined to retrieve such problems but noticeable caveats have been raised.

Given that (semi)-bold-line series has better convergence properties, we return to RPA series and proceed with an attempt for  $1/N_f$  expansions, with  $N_f$  being the number of fermion flavours. The initial impetus for this idea stemmed from the observation that  $N_f$  is independent of the dynamical parameters of the system and can be large even for real physical systems.

For real materials that  $1/N_f$  expansions would apply, there is a family of materials that Hund and exchange interactions are weak, typically in compounds when the  $d$ ,  $f$  orbitals are filled, *e.g.* ZnO. Such situations are common in wide band-gap semiconductors, while commonly adapted approaches are still based on DFT [10] or GW [1].

Compared to other bold-line schemes, *e.g.*  $G^2W$  [12],  $G^2\Gamma$  [13], *etc.*, the scheme we introduced does not require self-consistency at the DiagMC level but only when preparing tabulated bold-line building blocks. It is commonly agreed in the community that there is no misleading convergence for semi-bold diagrammatic series [14]. Compared to order-by-order RPA series, new features of the  $1/N_f$  expansions are that they change the diagram topologies by assigning higher priorities to diagrams with more closed fermion loops. With the  $N_f$  cut removed, the series returns to the order-by-order RPA series in the density-density channel while all the other bold-line series in the literature are in the particle-particle and particle-hole channels.

Besides a purely academic exposition for a new series, we applied the method to study Hubbard-type models beyond the square lattice. It is intriguing to ask if the convergence problem on honeycomb lattice may be solved by adapting existing bold-line algorithms, in particular RPADET [15] or CoS [16], the only two that admit exponential algorithms.

For RPADET, it is not easy to see how symmetry broken terms and additional fermion flavors could be added in the way that are consistent with the fast algorithm in [15]. For CoS, it is indeed mentioned in [16] that there can be a CoS-GW algorithm that could might solve the fermion flavours problem. However, no applications to any physical systems have been reported yet, especially for those that exhibit symmetry breaking of any kind.

Besides the obvious perspective of providing cross benchmarks, we aim to use this new series to study strongly-correlated physics. This would include both conventional  $SU(2)$  models and more exotic  $SU(N_f > 2)$  models. For  $SU(2)$  models, a multitude of outstanding questions remains to be addressed in systems with long-range interactions, frustrated lattice geometries, and stacked multi-layers structures. Such systems engender nontrivial complications for both numerically exact methods such as determinant quantum Monte Carlo and density-matrix renormalization group or heuristic methods such as dynamical mean field theories and its extensions.  $1/N_f$  expansions are anticipated to mitigate the limitations of these approaches in such contexts.

For  $SU(N_f)$  models, extensive numerical and experimental studies are still largely blank. Those models can directly simulate a box of atoms or molecules with high nuclear spins under external potentials, where there have been several preliminary experimental studies on ultracold alkali atoms [17, 18] in optical lattices. In periodic solids, such situations occur naturally in monolayer and stacked-bilayer graphenes, transition metals oxides, *etc.* Given that almost none of the real materials that have multiple orbits is on a square lattice with the ideal on-site Hubbard interactions, it is still a highly non-trivial task for the state-of-art CoS algorithm [16] to generalize to those scenarios.

Despite in this article we only present results with the density-density saddle-point, switching to mixed channels would share identical set of diagrams and employs analogous combinatorial algorithms. The more intriguing case is of course the cross of quantum phase transitions that are not adiabatically connected to this type of saddle point. We have seen evidence for the  $1/N_f$  expansion to cover those cases while the optimal truncation order can be learned and generalized.

As our second purpose, we also wish to reduce computational costs for more complicated situations. Even the leading-order corrections in  $1/N_f$  could furnish stable refinements to random-phase approximations, while the required CPU time is within minutes. Although the sign problem in equilibrium is manageable by other DiagMC algorithms, they would all struggle in non-equilibrium due to the additional exponential complexity in reaching long times. In disordered systems, many-body localizations would require an ensemble of thousands of systems copies generated from the distribution of disorders, where other DiagMC methods would require enormous computational resources.

The article proceeds as follows. In Sec. II, we give an overview of the Markov-Chain Monte Carlo methods we use. In Sec. III, we derive the  $1/N_f$  expansions in the framework of  $G - \Sigma$  functional theory. In Sec. IV, we give leading-order computations, higher-orders diagram generations, and low-rank decompositions for diagrams building blocks. In Sec. V, we apply the method to study  $t - t'$   $SU(2)$  and  $SU(6)$  Hubbard model on square and honeycomb lattices. In Sec. VI, we propose a combinatorial algorithm for optimizations.

## II. MARKOV-CHAIN MONTE CARLO METHODOLOGIES

There are in general two classes of algorithms in performing DiagMC, where the first treats the space of topologies and space(momentum)-time continuum vertices in the equal status and perform random walk in this space [19]. The second then firstly pre-generates all diagrams (or employs the determinant trick [15, 16, 20–25]) and merely performs random walks in the space of continuous parameters [16, 23, 26]. We will discuss the first approach in this section, suitable for low to intermediate orders. Further optimizations will be discussed later.

To quantify the sign problem, we define a norm as follows. For given  $\mathcal{N}$  diagrams, we insert  $\mathcal{M}$  boards between them and sum diagrams deterministically within adjacent boards. We perform random walks in  $(\mathcal{M}+1)$  group indices. Minimum of computational complexity then corresponds to the minimum of

$$S(\mathcal{Q}, \mathcal{P}) = \mathcal{C}(\mathcal{Q}, \mathcal{P}) \mathcal{A}(\mathcal{Q}, \mathcal{P})^2 \tau_f(\mathcal{Q}, \mathcal{P}), \quad (1)$$

where  $\mathcal{A}(\mathcal{Q}, \mathcal{P})$  is the integral of the absolute value of the function with partition  $\mathcal{Q}$  recording boards positions and permutation  $\mathcal{P}$  permuting diagrams ordering.  $\mathcal{C}(\mathcal{Q}, \mathcal{P})$  is the computational costs due to deterministic summation, which can be estimated during the execution.  $\tau_f(\mathcal{Q}, \mathcal{P})$  is the integrated auto-correlation time (IACT). In practice, the order of magnitude of the norm function and the IACT could be estimated with much less Monte Carlo iterations (*e.g.* the blocking method [27]), which renders minimization algorithms applicable, *e.g.* stimulated annealing [28].

To evaluate high-dimensional integrals arisen from Feynman diagrams, we combine the VEGAS algorithm [29, 30] and conventional Metropolis-Hastings algorithm for Markov-chain Monte Carlo [31, 32]. Consider

$$I = \int_{\mathbf{x} \in \Omega} f(\mathbf{x}) d\mathbf{x}. \quad (2)$$

The very peaky nature of the integrand could be retrieved to some extent by employing the VEGAS map. That is, a separable variable transformation,  $\{y_i(x_i)\}_{i \in \{1, \dots, \dim\}}$  is introduced by learning the integrand via iterations of plain Monte Carlo evaluations. In the transformed variable space,

$$I = \int_{\mathbf{y} \in [0,1]^{\otimes \dim}} f(\mathbf{x}(\mathbf{y})) J(\mathbf{y}) d\mathbf{y} \quad (3)$$

can be estimated by separating the sign and absolute value parts:

$$I = \mathcal{N} \int_{\mathbf{y} \in [0,1]^{\otimes \dim}} \text{sign}[\tilde{f}_{\mathcal{N}}(\mathbf{y})] |\tilde{f}_{\mathcal{N}}(\mathbf{y})| d\mathbf{y}, \quad (4)$$

where  $\dim$  is the dimension, normalization factor  $\mathcal{N} = \int_{\mathbf{y} \in [0,1]^{\otimes \dim}} |f(\mathbf{x}(\mathbf{y})) J(\mathbf{y})|$ , and  $\tilde{f}_{\mathcal{N}}(\mathbf{y}) = f(\mathbf{x}(\mathbf{y})) J(\mathbf{y}) / \mathcal{N}$ . Convergence for paralleling multiple Markov chains was checked by the blocking method [27] and the Gelman-Rubin statistics [33]. We give more details of the parameters used for MCMC in Appendix. D.

For models with contact interactions, screened interactions contain a contact part with bare  $U$  and a dynamical part, which enlarges the Monte-Carlo variance. The switch between them introduces empty time vertices on which the integrand does not explicitly depend. One may observe that the compensation trick introduced in [34] just amounts to fill in those empty nodes with the suggested vertex function in [34]. We showed in the subsequent sections that one may further integrate out internal time vertices with the aid of low-rank decomposition. However, we found the numerical stability is much better with compensation trick only when taking numerical derivatives (discussed in Appendix. D). And therefore for density and energy computations we use the compensation trick only.

## III. THEORETICAL FRAMEWORK

We consider the  $SU(N_f)$  Hubbard model in generic lattices. The (normal ordered) Hamiltonian is

$$H = - \sum_{\langle i,j \rangle, m} t_{ij} (c_{i,m}^\dagger c_{j,m} + \text{H.c.}) - \mu \sum_{i,m} c_{i,m}^\dagger c_{i,m} + \frac{1}{2N_f} \sum_{i,j,m,m'} v_{\alpha\beta}(i,j) c_{i,m,\alpha}^\dagger c_{j,m',\beta}^\dagger c_{j,m',\beta} c_{i,m,\alpha}, \quad (5)$$

where  $i, j$  denote unit cell positions,  $\alpha, \beta$  denote lattice sites in one unit cell and  $m, m'$  are flavour indices, and bold symbols for  $c$  and  $c^\dagger$  denote a vector of spin-up and spin-down creation and annihilation operators. Hopping integrals and interactions are not specified at this stage but could be of various types, *e.g.* NN in the honeycomb lattice.

In the presence of spontaneous spin-rotation symmetry breaking, Green's functions are not homogeneous over different spins. As a scrupulous choice, we reformulate the fermionic path integral in the  $G - \Sigma$  functional theory [35, 36], where the field degrees of freedom is the spin-averaged bosonic fields. The action is given by

$$\begin{aligned}
S = & \int_{\tau, \tau', i, j} \bar{\psi}_m(i, \tau) \delta(\tau - \tau') [(\partial_\tau - \mu) \delta_{ij} + h_{ij}] \psi_m(j, \tau') + \frac{N_f}{2} \int_{\tau, \tau', i, j} \delta(\tau - \tau') G_{\alpha\alpha}(i, i, \tau, \tau') G_{\beta\beta}(j, j, \tau, \tau') v_{\alpha\beta}(i, j) \\
& - N_f \int_{\tau, \tau', i, j} \Sigma_{\beta\alpha}(j, i; \tau', \tau) \left[ G_{\alpha\beta}(i, j; \tau, \tau') - \frac{1}{N_f} \sum_{m=1}^{N_f} \psi_{\alpha, m}(i\tau) \bar{\psi}_{\beta, m}(j, \tau') \right],
\end{aligned} \tag{6}$$

where  $h_{ij}$  are hopping matrix elements. We have introduced a pair of bilinear fields,  $G$  and  $\Sigma$  to reformulate the original action [37]. We now introduce the compact index notation  $1 = (\tau, i, \alpha)$ . After integrating out the fermionic fields, the effective action for  $G$  and  $\Sigma$  is

$$\frac{S[G, \Sigma]}{N_f} = -\text{Tr} \ln[G_0^{-1} - \Sigma] - \int_{1,2} \Sigma(1,2) G(2,1) + \frac{1}{2} \int_{1,2,3,4} G(1,2) G(3,4) v(2,3) \delta_{1,2} \delta_{3,4}. \tag{7}$$

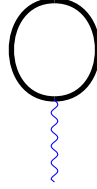
To the leading order in  $1/N_f$ , the saddle point equation  $\delta S/\delta G = 0$  and  $\delta S/\delta \Sigma = 0$  is a self-consistent Hartree equation and the Dyson's equation, namely

$$\Sigma_*(1,2) = \int_{3,4} v(1,3) G(3,4) \delta_{1,2} \delta_{3,4} \tag{8}$$

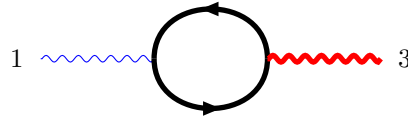
and

$$G_* = [G_0^{-1} - \Sigma_*]^{-1}. \tag{9}$$

This coincides with the naïve power counting, with the Feynman diagram being the Hartree diagram,



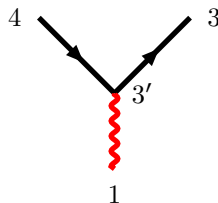
We expand the  $G - \Sigma$  action around the saddle point to quadratic order with the fluctuation field  $G = G_* + \delta G$ ,  $\Sigma = \Sigma_* + \delta \Sigma$  using the functional Taylor expansion, where the four second-order derivatives can be easily computed. Propagators between bi-linear fields can then be computed, where we denote them as  $G_{\delta\Sigma\delta\Sigma}$  and  $G_{\delta\Sigma\delta G}$ . One may readily realize that  $G_{\delta\Sigma\delta\Sigma}$  plays the same role as the screened interactions in the random-phase approximation (RPA)  $G_{\delta\Sigma\delta\Sigma}(1,2;3,4) \equiv W(1,3) \delta_{1,2} \delta_{3,4}$ , where  $\delta W(1,3) = W(1,3) + v(1,3)$  is graphically represented as



The thin wiggly line is bare interaction vertex,  $v$ , bold wiggly line is  $W$ , and the bold solid directed line is  $G_*$ . One can similarly show that

$$G_{\delta\Sigma\delta G}(1,2;3,4) = -\delta_{4,1} \delta_{3,2} - \delta_{1,2} \int_{3'} W(1,3') G_*(4,3') G_*(3',3), \tag{10}$$

with the second part graphically represented as



Beyond the quadratic order, one may expand the effective action as:

$$S = N_f S_* + \sum_{n=2}^{\infty} N_f S_n[\delta\Sigma, \delta G]. \quad (11)$$

After rescaling the fields and expanding the trace log, interacting parts in the action are given as

$$S_I = \sum_{n=3} \frac{1}{n} N_f^{1-n/2} \text{Tr}[(G_* \delta\Sigma)^n]. \quad (12)$$

At this stage, one may realize the close relation between systematic  $1/N_f$  expansion and the RPA series. The extra one in the power of  $N_f$  effectively counts the number of closed fermion loops, each of which carries a factor of  $N_f$ . While in the RPA series, one may just count the number of  $\delta\Sigma$  in a diagram, and the number of screened interactions would be half of that.

The change in topology in those two sibling schemes results in drastic difference between the number of diagrams in each order. E.g., at the second order in  $1/N_f$  expansion, four  $n = 3$   $G - \Sigma$  vertices has six screened interactions and four closed fermion loops, while that can only occur at the sixth order in the RPA series. The pattern in the interaction vertices was then used to build all diagrams.

#### IV. DATA PREPARATION, LEADING ORDERS AND GRAPHICS

The first step is to solve the self-consistent Hartree equation. The Dyson's equation for the Matsubara Green's function [38] with only the Hartree self-energy as

$$\left[ \frac{d}{d\tau} + h \right] G(\tau) = \delta(\tau) + \Sigma_H[G(-\epsilon)]G(\tau). \quad (13)$$

Eq. (13) can be efficiently solved using the `newton-krylov` method for large number of unit-cells.

In momentum space, the integral equation for the screened interactions is (indices suppressed)

$$W(\tau, \mathbf{k}) = -v(\mathbf{k})\delta(\tau) + \frac{1}{\sqrt{N_1 N_2}} \int_{\tau'} v(\mathbf{k}) P(\tau - \tau', \mathbf{k}) W(\tau', \mathbf{k}), \quad (14)$$

where the polarization matrix is

$$P_{b'c}(\tau - \tau', \mathbf{k}') = \sum_{\mathbf{k}'} G_{*b'c}(\tau - \tau', \mathbf{k}) G_{*,cb'}(\tau' - \tau, \mathbf{k}' - \mathbf{k}). \quad (15)$$

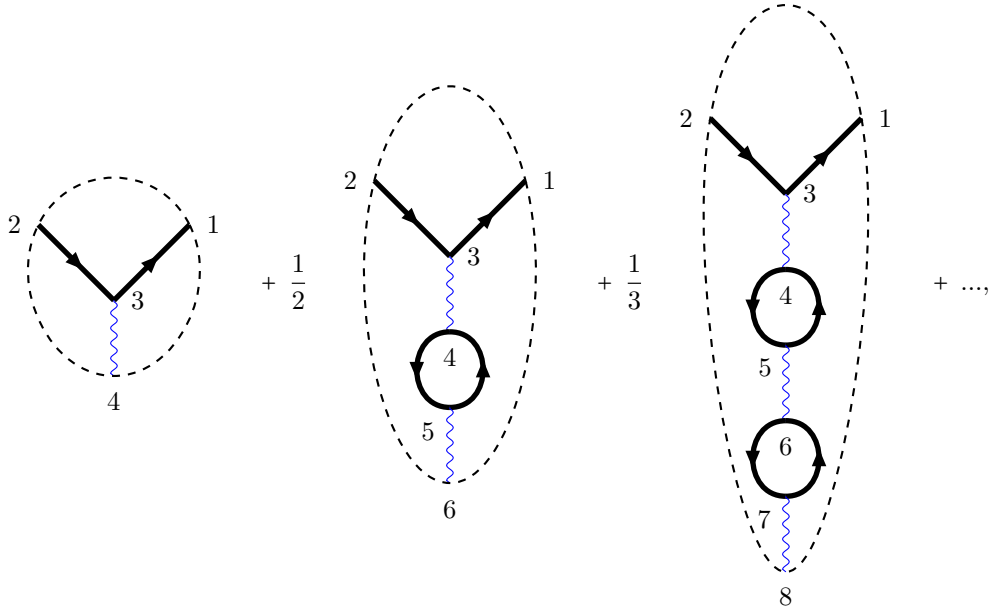
In practice, it is useful to separate out the singular part of  $W(\tau, \mathbf{k}) = -v(\mathbf{k})\delta(\tau) + \delta W(\tau, \mathbf{k})$ , where  $\delta W(\tau, \mathbf{k})$  satisfies

$$\delta W(\tau, \mathbf{k}) = -\frac{1}{\sqrt{N_1 N_2}} v(\mathbf{k}) P(\tau, \mathbf{k}) v(\mathbf{k}) + \frac{1}{\sqrt{N_1 N_2}} v(\mathbf{k}) \int_{\tau'} P(\tau - \tau', \mathbf{k}) \delta W(\tau', \mathbf{k}). \quad (16)$$

The saddle point contribution to  $\ln Z$  is directly evaluated from the action. The  $\mathcal{O}(N_f^0)$  (next order to the saddle point) contribution to  $\ln Z$  is evaluated from the functional determinant

$$\ln Z^{(1)} = -\frac{1}{2} \text{Tr} \ln(\mathbb{I} - K_G), \quad (17)$$

where  $K_G(1, 2; 3, 4) = \mathcal{f}_{3'} v(3', 3) G_*(3', 2) G_*(1, 3') \delta_{3,4}$ . RHS of Eq. (17) can be graphically represented as



where loosely connected circles denote space-time integration. A trick to evaluate the functional determinant is to introduce an auxiliary variable  $x$  such that

$$v \sum_{n=0}^{\infty} \frac{1}{n} (P \circ v)^n = \int_0^1 v \sum_{n=0}^{\infty} x^n (P \circ v)^n dx. \quad (18)$$

And thus a self-consistent integral equation for  $\delta W_x(\tau, \mathbf{k})$  is formed akin to Eq. (16), with  $x$  multiplied on the RHS.

From low to intermediate orders, it is better to adopt the approach that all diagrams are pre-generated. This procedure was benchmarked by checking the weight factor of individual diagrams for Green's functions cancelled with its multiplicity via topological filtering [39–41], while for free-energy diagrams, symmetry factors do exist and we found that it matched with textbook results for lowest order diagrams. Also, integrals with filtered and unfiltered graphs were compared to be matched. Large graphs matches were employed using the VF2 algorithms [39–41].

Each edge of the diagram is assigned with a momentum and an imaginary time. We picked up a number of free momentum based on the rank of the momentum conservation equations (similar approach to that used in [26]) and a number of free time based on the fact that time sums to zero for each closed loop, where extra attention has to be paid for the contact/non-contact interaction switch, as in Eq. (14).

For sufficient higher orders, the factorial decrease of the average sign becomes a central issue of the simulation [42] by sampling diagrams individually. Previous approaches employing the determinant trick [15, 16] with bold-line series may apply to  $1/N_f$  expansions due to the additional requirement for partitioning the number of closed fermion loops. We will discuss our combinatorial optimizations later, but focus on preparing building blocks in this section. Non-local vertices in each diagram can be integrated to retrieve the problem of more spread of vertices and use the two-point  $\mathcal{L}$  functions as building blocks, defined as:

$$\mathcal{L}_{abc}(\tau_1, \tau_2, \mathbf{k}, \mathbf{k}') = \sum_d \int_{\tau'} G_{*,ad}(\tau_1 - \tau', \mathbf{k}) G_{*,dc}(\tau' + \tau_2, \mathbf{k}') W_{db}(\tau', \mathbf{k} - \mathbf{k}'). \quad (19)$$

Its storage is a practical issue for memory usage, where we used the discrete-Lehmann representation [43, 44]

$$W_{ab}(\tau, \mathbf{k}) = \sum_{l=1}^{r(\beta)} \hat{W}_{ab}(\omega_{l,ab}(\mathbf{k}), \mathbf{k}) e^{-\omega_{l,ab}(\mathbf{k})\tau}. \quad (20)$$

Since the analytical form of Green's function in momentum space is known, the complexity for single function call only scales as  $\mathcal{O}(r)$ . We give more details on discrete Lehmann representations and computations of the  $\mathcal{L}$  function in Appendix. B. Since bold-line diagrams are not organized in the particle-particle or particle-hole channels as in [15], the cover by  $\mathcal{L}$  is not full, and thus there would be remaining fermion and screened interaction lines left.

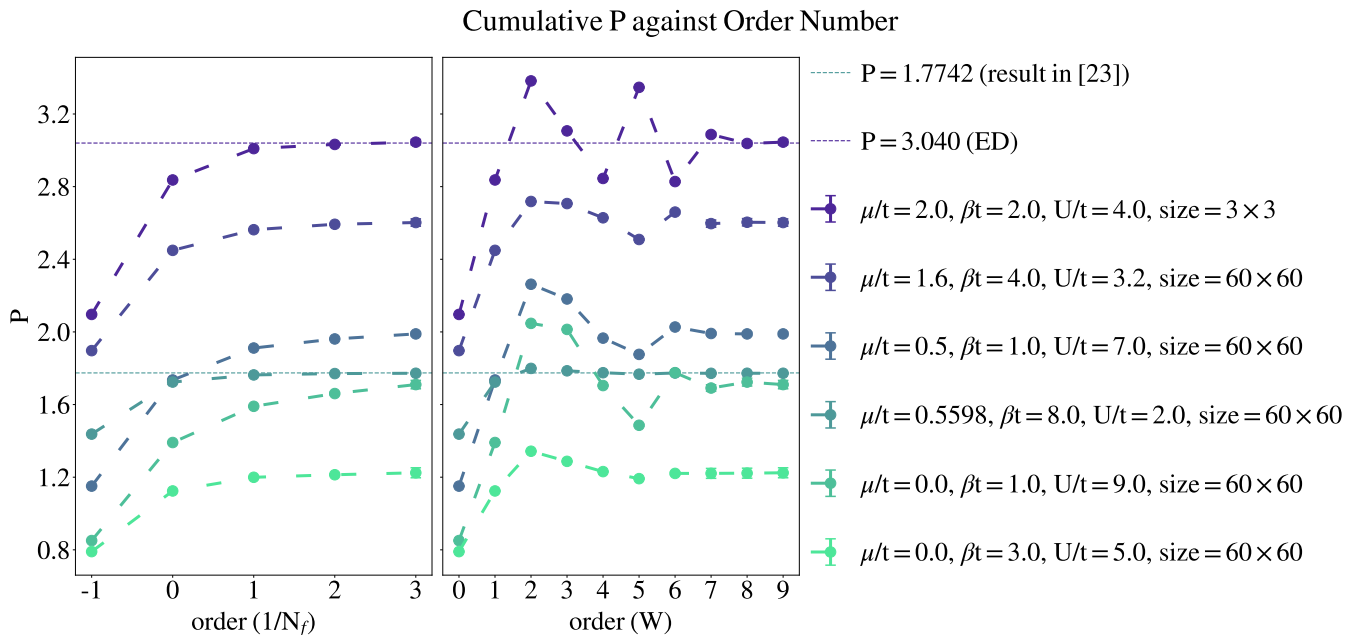


FIG. 1. Cumulative pressure (partial summed pressure cumulating order-by-order contributions) against  $1/N_f$  orders and  $W$  orders with  $N_f$  cut being 3. For small systems, pressure is not well defined. We use the definition  $P = \ln Z / (\beta N_1 N_2)$  for plots. Two benchmarks were done with exact diagonalization (ED) for  $3 \times 3$  systems and CDet for  $60 \times 60$  systems drawn from [23]. CDet gives [23] 1.7742 while  $1/N_f$  gives 1.7723(9). ED was performed using the `QuSpin` package [47, 48]. We also simulated a rather trivial parameter value  $U/t = 5$ ,  $\mu/t = 10$ ,  $\beta t = 0.5$  for  $3 \times 3$  system, which gives  $\ln Z = 7.704(4)$  compared with exact value  $\ln Z = 7.7128$ . Parameters are shown on the rightmost legend. The LHS plot shows series in powers of  $1/N_f$  while RHS plot shows series in powers of  $W$ . Order 9 is the maximal diagrams order with powers of  $1/N_f$  less than or equal to 3, and thus the final result gives the full third-order (with respect to free energy)  $1/N_f$  expansion.  $-1$  on LHS and  $0$  on RHS label the saddle point. Each point in the LHS plot sums several orders in  $W$  series with  $N_f$ ;  $\mathcal{O}(1/N_f)$  spans orders 2 to 3 in  $W$ ,  $\mathcal{O}(1/N_f^2)$  spans orders 3 to 6 in  $W$ , and  $\mathcal{O}(1/N_f^3)$  spans orders 4 to 9 in  $W$ .

## V. EXAMPLES

### A. 2D SU(2) Hubbard Model on Square Lattice

We firstly benchmarked the correctness of the simulation with exact diagonalization for grand-canonical potential density in  $3 \times 3$  square lattice with the SU(2) Hubbard model, shown in the Fig. 1. There is a further large system benchmark compared with the CDet result [23]. Several other double-blind parameters in Fig. 1, demonstrating its ability to make realistic predictions.

It was conjectured by Lee in [45] that naïve  $1/N_f$  power counting would be uncontrolled for non-fermi liquids coupled with U(1) gauge fields at  $T = 0$ . However, there are two potential caveats of Lee's arguments in [45]. It starts with the one-loop quantum effective action and finds an action that could reproduce it. It is not clear if the starting point is entirely correct. Secondly, it shows an infinite number of planar diagrams, but may cancel to a very small value. Enduring discussions and debates seems to enlarge the connotations of Lee's analysis to equivocation, which severs the applicability of naïve  $1/N_f$  counting from any non-fermi liquid.

Nevertheless, we show numerically that, for half-filled non-fermi liquids phases for the Hubbard model at finite temperature [46], the  $1/N_f$  series exhibits exponential convergence for  $\ln Z$ , as plotted as the in Fig. 1, with  $\mu/t = 1.6$ ,  $\beta t = 4.0$ ,  $U/t = 3.2$ .

We also provide benchmarks at low filling with results in [49]. We consistently found significant improvements of results using a symmetric Borel-Padé approximation, reflecting the power-law nature of the singularity in the complex  $1/N_f$  plane in this regime.

$t'$	$n$	U	$\beta$	DCA			DiagMC-GF		Borel-Padé $\mathcal{O}(1/N_f^2)$	
				# sites	$E$	$\delta E$	$E$	$\delta E$	$E$	$\delta E$
0	0.3	12	4	20	-0.821	0.013	–	–	-0.849	0.017
0	0.3	8	4	32	-0.824	0.004	–	–	-0.864	0.010
-0.2	0.6	6	2	50	-0.874	0.010	–	–	-0.886	0.014
0	0.3	4	4	34	-0.8549	0.0002	-0.8574	0.0007	-0.8605	0.007
0	0.3	6	4	34	-0.836	0.002	-0.841	0.002	-0.845	0.004

TABLE I. Benchmarks on total energy computations between Borel-Padé  $\mathcal{O}(1/N_f^2)$ , (*i.e.* resum the saddle-pt, RPA,  $\mathcal{O}(1/N_f)$ ,  $\mathcal{O}(1/N_f^2)$  using the Borel-Padé re-summation with the symmetric rational polynomials.), dynamical cluster approximations (DCA), and GF diagrammatic Monte Carlo. For DCA, we also give the number of sites of the cluster.  $n$  represents the filling fraction and  $t'$  is the second-nearest neighbor hopping amplitude.

### B. 2D SU(2) Hubbard model on Honeycomb Lattice

On honeycomb lattice, we used the state-of-art symmetry broken perturbation series introduced in [50, 51] combined with fast principal minor algorithms for cross-benchmark. Since it is for the first time this method is applied, we also give detailed technical steps.

Consider generic bipartite lattices with sub-sites A and B. To increase the radius of convergence, we perform chemical potential plus staggered magnetization shifts, which effectively takes both semi-metal and anti-ferromagnetism behaviors into account. The one-body Hamiltonian becomes (honeycomb lattice with nearest-neighbor hopping)

$$\sum_{\sigma=\uparrow,\downarrow} c_{\sigma}^{\dagger}(\mathbf{k}) \begin{pmatrix} \Delta_{\sigma} - (\mu - \alpha_{\sigma}) & \epsilon(\mathbf{k}) \\ \epsilon^{*}(\mathbf{k}) & -\Delta_{\sigma} - (\mu - \alpha_{\sigma}) \end{pmatrix} c_{\sigma}(\mathbf{k}), \quad (21)$$

where the hopping energy  $\epsilon(\mathbf{k}) = -(1 + e^{i\mathbf{k}\cdot\mathbf{b}_1} + e^{i\mathbf{k}\cdot\mathbf{b}_2})$  and  $\Delta_{\sigma}$ ,  $\alpha_{\sigma}$  are shift parameters. To compensate the shifts, Green's functions with shifted parameters at equal space/time in the determinant (discussed below) are further shifted by

$$\begin{aligned} g_{\sigma}^{AA}(0^{-}, \mathbf{R}_i, \mathbf{R}_i) &= g_{\sigma}^{AA}(0^{-}, \mathbf{R}_i, \mathbf{R}_i) + (\alpha_{\bar{\sigma}} + \Delta_{\bar{\sigma}})/U \\ g_{\sigma}^{BB}(0^{-}, \mathbf{R}_i, \mathbf{R}_i) &= g_{\sigma}^{BB}(0^{-}, \mathbf{R}_i, \mathbf{R}_i) + (\alpha_{\bar{\sigma}} - \Delta_{\bar{\sigma}})/U, \end{aligned} \quad (22)$$

where  $\bar{\sigma}$  is the opposite spin to  $\sigma$ . In our numerical examples, we did not choose the shift parameters exactly corresponding to the mean field values to test the robustness of the shifts. Contributions to the partition function  $Z$  at order  $m$  is (powers of U suppressed)

$$Z^{(m)} = \frac{1}{m!} \oint_{a_1, \dots, a_m}^{x_1, \dots, x_m} \prod_{\sigma} \det \left[ \begin{matrix} X_1, \dots, X_m \\ X_1, \dots, X_m \end{matrix} \right]_{\sigma}^{\{a_{i's}\}}, \quad (23)$$

where

$$\left[ \begin{matrix} X_1, \dots, X_m \\ X_1, \dots, X_m \end{matrix} \right]_{\sigma}^{\{a_{i's}\}} = \begin{vmatrix} g_{\sigma}^{a_1 a_1}(X_1, X_1) & \dots & g_{\sigma}^{a_1 a_m}(X_1, X_m) \\ \vdots & \ddots & \vdots \\ g_{\sigma}^{a_m a_1}(X_m, X_1) & \dots & g_{\sigma}^{a_m a_m}(X_m, X_m) \end{vmatrix}. \quad (24)$$

One can readily realize that the summation over all internal sub-lattice sites is just the sum of all the principal minors of the  $2m \times 2m$  axillary matrix with column and row indices formed by  $(X_1, A)$ ,  $(X_1, B)$ ,  $\dots$ ,  $(X_m, A)$ ,  $(X_m, B)$ . A simple modification of the fast principal minor algorithm would compute the sub-lattice sum in  $\mathcal{O}(2^m)$  operations [25]. Recursive removal of disconnected diagrams follows the standard procedure in [23].

One can directly compute, for example, the spin-up Green's function as well using the following recipe (external points are denoted by  $(X, a)$  and  $(X', a')$ .  $a = 0, 1(A, B)$ ). First, remove the XOR columns and rows for the spin-up matrix, *i.e.*  $M[\bar{a}] = \mathbf{0}$ ,  $M[:, a'] = \mathbf{0}$ . (No sum on external sub-lattice indices.). Then, swap the  $a$  and  $a'$  rows if  $a \neq a'$ . (Principal minors select the same row and columns indices.). In the following, add a  $2 \times 2$  identity block to the upper left of the spin-down matrix. Finally, use exactly the same principal minor summation function to proceed.



We managed to reduce the single MCMC update time for  $\ln Z$  at order nine to around 0.02s (single CPU core). And thus we are able to reach the 10<sup>th</sup> order in perturbation series.

We found the performance of shifted bare-U series strongly depending on the shift parameters even at rather high temperatures and weak interactions. We performed benchmarks of this method via exact diagonalization (ED) at  $2 \times 2$  lattice and at  $8 \times 8$  lattice with determinant quantum Monte Carlo (DQMC). We started with rather high temperature at  $U/t = 2$ ,  $\beta t = 2$  for  $2 \times 2$  lattice. Density computation could match with the exact result to nearly five decimal places. However, at the same set of parameters as the left-hand plot in Fig. 2, the shifted bare-U series gives  $\ln Z = 4.2664$  which is far below the exact value 5.2664. All the proceeding orders give small corrections which “misleads” the Padé approximant. Nevertheless, the  $\mathcal{O}(1/N_f)$  series can perfectly recover the exact value. Interestingly, we compute density as  $n = \frac{1}{\beta} \frac{\partial \ln Z}{\partial \mu}$ , which uses exactly the same integrand as free energy computation. This might signify that this method is only numerically controlled at some directions since free energy contains essentially all the thermodynamical information of the system. More benchmarks with DQMC is given in Appendix. A.

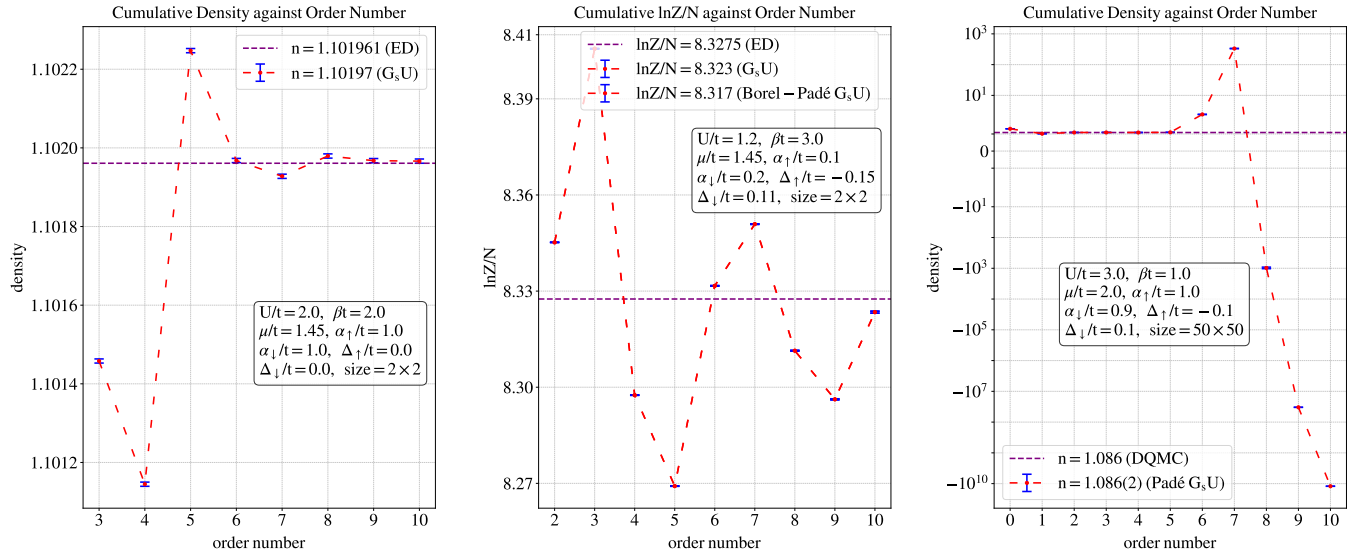


FIG. 2. Cumulative order-by-order density (left), grand potential density (middle) on  $2 \times 2$  honeycomb lattice and order-by-order density (right) on  $50 \times 50$  honeycomb lattice using shifted bare-U series, with all the dynamical and shift parameters given in the text box in the plot. Exact value computed via exact diagonalization for small systems using QuSpin [47, 48] shown at the top right corner. G<sub>s</sub>U in the legend box means naïve sum of order-by-order corrections. For the right plot, the series is wildly divergent while (5, 5) Padé approximation could give accurate prediction (second line in the bottom left box of the right plot), consistent with DQMC and  $1/N_f$  results.

In Table. II, we provide benchmarks between the  $1/N_f$  expansion and determinant quantum Monte Carlo (DQMC). The DQMC simulations were performed using the SmoQyDQMC package in Julia [52]. The  $\mathcal{O}(1/N_f)$  order gives robust correction. Despite only being a toy model,  $2 \times 2$  systems also exhibit many strongly correlated physics. As can be seen from the top six lines, accuracy when crossing the semi-metal to antiferromagnetic Mott transition is not affected significantly. The same also applies when lowering the temperature. Just as the opposite, we usually found large systems are much easier to be simulated than small clusters due to the smoothness of momentum distribution.

In addition, we also give independent predictions of the grand-potential per site for large system, which we usually found the shifted bare-U series gave the fluctuating answers for different shift parameters. Pressure measurements to verify the theoretical results are within current cold-atom platforms, though the temperature is challenging to be reached experimentally.

### C. 2D SU(6) Hubbard Model on Square and Honeycomb Lattices

We show in Table. III comparisons of density computations between the CoS results in [16] and the truncated  $1/N_f$  results. As the interaction and filling increase, there is a proliferation of error bars in CoS and also in the  $1/N_f$  expansion. When both are able to tighten errors at weak coupling, there is a perfect match between the two methods.

U/t	$\mu/t$	$\beta t$	Quantity	Size	DQMC/ED	Saddle Pt	RPA	$\mathcal{O}(1/N_f)$	$\mathcal{O}(1/N_f^2)$	Sum
5	1	5	$\ln Z/N$	$2 \times 2$	8.498	4.9046	2.3251	1.025(1)	–	8.255(1)
5	2.5	5	$\ln Z/N$	$2 \times 2$	15.700	9.1325	4.6361	1.405(3)	–	15.174(3)
5	3.5	5	$\ln Z/N$	$2 \times 2$	20.749	12.9695	6.2621	1.481(3)	–	20.713(3)
6	1.5	5	$\ln Z/N$	$2 \times 2$	10.402	5.5225	3.0109	1.400(2)	–	9.933(2)
8	4.6	8	$\ln Z/N$	$2 \times 2$	40.301	20.1859	13.2258	4.56(5)	–	37.97(5)
8	5	12	$\ln Z/N$	$2 \times 2$	65.212	33.4798	21.8963	6.98(5)	–	62.36(5)
3	1	2	density	$4 \times 4$	0.918	0.6823	0.2003	$2.966(4) \times 10^{-2}$	$-2.5(26) \times 10^{-5}$	0.912(1)
4	-1.42	6	density	$8 \times 8$	0.355	0.2165	0.1103	$2.439(6) \times 10^{-2}$	$2.6(9) \times 10^{-3}$	0.353(2)
5	-2	5	density	$8 \times 8$	0.221	0.1220	0.08230	$2.538(7) \times 10^{-2}$	$4.2(4) \times 10^{-3}$	0.234(1)
4	-1	6	$\ln Z/N$	$50 \times 50$	–	1.7069	0.8960	$1.964(7) \times 10^{-1}$	$1.96(33) \times 10^{-2}$	2.819(3)
5	-1	8	$\ln Z/N$	$50 \times 50$	–	1.9594	1.2773	$3.338(31) \times 10^{-1}$	$5.1(17) \times 10^{-2}$	3.62(2)
7	0	6	$\ln Z/N$	$50 \times 50$	–	2.6854	2.1085	$7.836(40) \times 10^{-1}$	$1.8(13) \times 10^{-1}$	5.8(1)

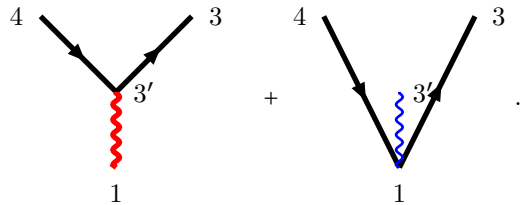
TABLE II. Benchmarks the  $1/N_f$  method with DQMC and exact diagonalization for SU(2) Hubbard model on honeycomb lattice. For  $2 \times 2$  systems, we used exact diagonalization while for  $4 \times 4$  and  $8 \times 8$  systems we used DQMC. In DQMC, we have varied trotterization in time ( $\Delta\tau = 0.1, 0.05, 0.03, 0.025$ ) and number of bins ( $N_{\text{bin}} = 50, 70$ ) for MCMC blocking to check convergence. We found for density computations where there exhibits fast convergence Borel-Padé re-summation only finely modifies the results.

When it enters the strongly correlated regime, at some filling fractions there are larger differences. We investigated parameter values at  $U/t = 8$ ,  $\mu/t = 1.746251$ ,  $T/t = 0.15$  and found significant finite-size effects. We conjecture that there is a weak second-order phase transition near this filling.  $\mathcal{O}(1/N_f)$  expansion is already highly accurate away from the phase transitions and provides decent corrections beyond the RPA results. Importantly, the approximate point of phase transitions can be probed via finite-size effects scaling, where adding the second-order in  $1/N_f$  or even higher in perturbation series is required.

In Fig. 3, we also provide equations of states data for  $U/t = 4, 6, 7, 10, 13$  at low temperature  $\beta t = 7$  on honeycomb lattice. To our knowledge, there have not been systematic studies of this model in the literature. We did not spot drastic changes of series convergence when switching lattice geometry in this regime of parameters. Similar to the square lattice case, compressibility becomes lower when interactions becomes stronger, indicating the Mott tendency.

## VI. A SCHEME OF COMBINATORIAL OPTIMIZATION

As mentioned in Sec. II, the compensation trick groups diagrams by the building blocks



(The bold red line is now  $\delta W$  not  $W$ .) The internal time indices at  $3'$  can be integrated out using the discrete Lehmann representation. Even with internal time vertices not integrated out, we already found hundreds of or even thousands of times speed up at high orders ( $\gtrsim 6$ ) compared with the naïve approach with a contact/non-contact update. The  $\mathcal{L}$  cover is not full and we use the cover that has maximum number of  $\mathcal{L}$  functions.

In this section, we propose another scheme of combinatorial optimization, not only for  $1/N_f$  expansions but for general mixed channel RPA series as well since they share similar sets of Feynman diagrams. Previous bold-line RPA series [15] are formed in particle-particle and particle-hole channels. In those channels, there always exists a full cover

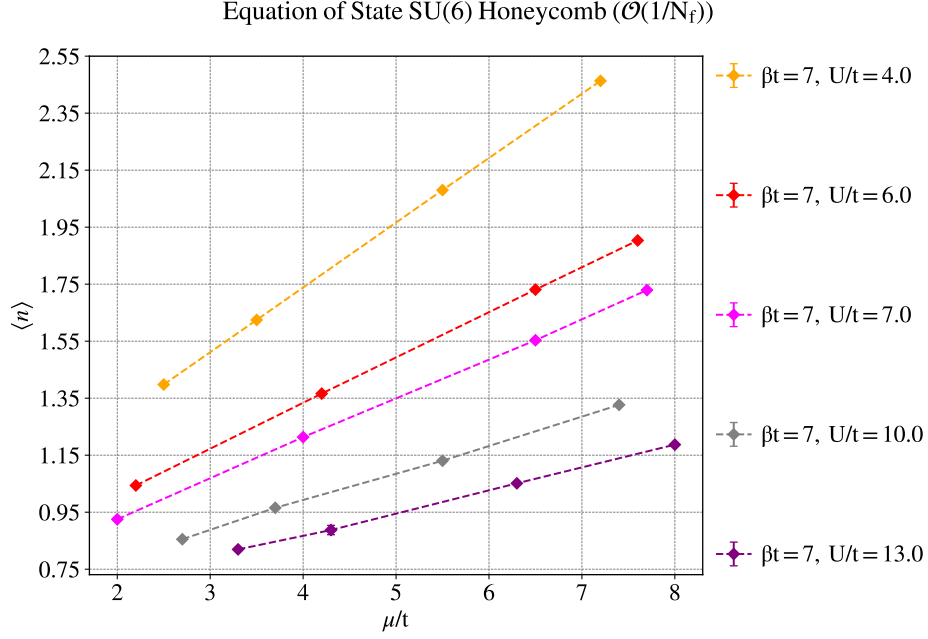


FIG. 3. Equation of state for SU(6) Hubbard model on  $50 \times 50$  honeycomb lattice for different interacting strength. All the results are obtained by summing the saddle point, RPA and  $\mathcal{O}(1/N_f)$  orders.

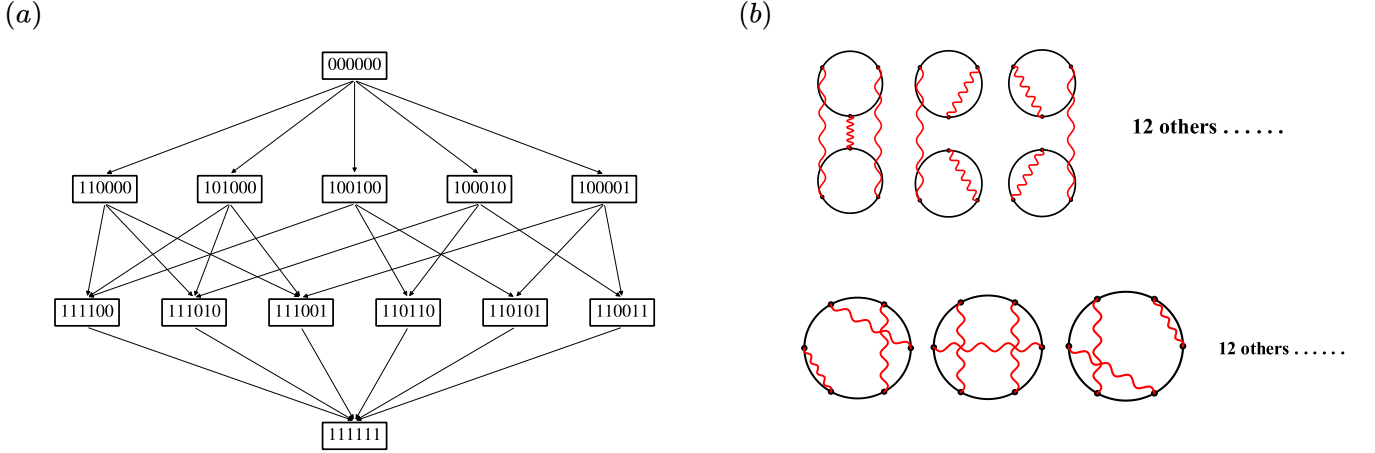


FIG. 4. Bold-line Feynman diagrams with three screened interactions and the corresponding call graph. This figure assumes all the interactions are non-contact and works in real space. We present modifications of contact/non-contact switch in the main text. There are two different partitions (6, ) and (3, 3). 0's in the call graph nodes represent vertices that are not connected by a screened interaction while 1's represent vertices that are already connected by a screened interaction. Each edge is a screened interaction.

of  $\mathcal{L}$  functions and fast algorithms are based on determinants. In our case, if there is no contact/non-contact switch, all the Feynman diagrams within a partition  $(n_1, n_2, \dots)$  with  $n_i \geq 3$  are just perfect matchings in a complete graph with  $\sum_i n_i$  nodes. Feynman diagrams can be organized efficiently in a call graph as shown in Fig. 4. The call graph can be constructed at arbitrary orders using the following rules. The first layer only has one node which is  $[00\dots 0]$ . The last layer only has one node which is  $[11\dots 1]$ . There are  $n$  layers in total. The first  $j$  digits for all nodes in the  $j^{\text{th}}$  ( $j = 0, \dots, n - 1$ ) layer are all 1's. Nodes at the  $j^{\text{th}}$  layer have  $2j$  1's in total. Inter-layer connections are defined as: a node B in the  $(j + 1)^{\text{th}}$  layer is connected to a node A in the  $j^{\text{th}}$  layer if 0's in B are in 0's in A; 1's in A are in 1's

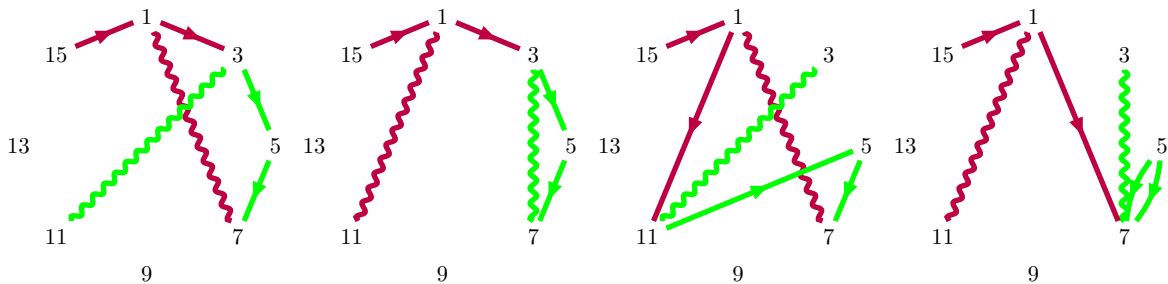
$\mu/t$	U/t	CoS	$1/N_f$		
		$n$	saddle-pt	RPA	Sum $\mathcal{O}(1/N_f)$
-2.300000	2.3	0.4868(50)	0.39798	0.08224	0.487
-1.725000	2.3	0.6506(5)	0.53662	0.10378	0.651
-1.150000	2.3	0.8178(9)	0.67783	0.12418	0.815
0.000000	2.3	1.1515(12)	0.96806	0.16276	1.148
0.575000	2.3	1.3215(14)	1.11728	0.18126	1.318
1.725000	2.3	1.666(3)	1.42457	0.21729	1.665
-1.679207	4.0	0.5340(25)	0.38851	0.12463	0.533(1)
-0.886256	4.0	0.7021(26)	0.52397	0.15178	0.700(1)
-0.088440	4.0	0.877(4)	0.66202	0.17616	0.865(1)
0.714382	4.0	1.040(5)	0.80267	0.19854	1.030(1)
1.522465	4.0	1.201(6)	0.94604	0.21938	1.195(1)
2.336111	4.0	1.367(7)	1.09224	0.23899	1.360(1)
3.155679	4.0	1.532(12)	1.24145	0.25759	1.530(1)
3.981595	4.0	1.694(16)	1.39384	0.27547	1.704(2)
-0.218517	8.0	0.635(15)	0.37908	0.18969	0.623(2)
1.087260	8.0	0.808(18)	0.51151	0.22081	0.781(3)
1.746251	8.0	0.900(15)	0.57872	0.23438	0.866(4)
2.409349	8.0	0.995(15)	0.64660	0.24695	0.941(3)
3.076639	8.0	1.045(15)	0.71515	0.25867	1.021(3)
3.748223	8.0	1.120(25)	0.78440	0.26967	1.098(4)
5.104735	8.0	1.245(45)	0.92502	0.28991	1.263(4)
6.479902	8.0	1.399(45)	1.06863	0.30825	1.417(6)
7.874923	8.0	1.555(55)	1.21540	0.32510	1.566(7)
9.291230	8.0	1.695(70)	1.36554	0.34081	1.759(8)
1.242173	12.0	0.720(35)	0.37508	0.23023	0.674(5)
3.980462	12.0	0.962(25)	0.57287	0.27468	0.92(1)
4.442917	12.0	0.985(30)	0.60643	0.28085	0.95(1)
5.840947	12.0	1.085(40)	0.70813	0.29787	1.06(1)
8.687005	12.0	1.25(10)	0.91637	0.32685	1.30(1)
10.623692	12.0	1.38(10)	1.05898	0.34347	1.44(2)
14.600865	12.0	1.64(14)	1.35416	0.37237	1.75(2)

TABLE III. Density benchmarks for SU(6) Hubbard model on the square lattice with the Hartree-shifted bare-U series implemented by the CoS algorithm in [16]. The  $\mathcal{O}(1/N_f)$  represents the results by summing saddle-point, RPA and  $\mathcal{O}(1/N_f)$  correction for  $70 \times 70$  system. Temperature is set at  $T/t = 0.15$ , the lowest attempted in [16]. The last column represents summing the saddle point, RPA and  $\mathcal{O}(1/N_f)$  order. Directly summing the fourth and fifth columns would give the saddle point plus RPA corrections.

in B; The first position for 1's in B that are not in A must start from the first position of 0 in A. Number of edges (=number of multiplication) has good scalability between  $\mathcal{O}(n^3 2^n)$  and  $\mathcal{O}(3^n)$ , where there are 6, 26, 97, 332, 1076, 3361, 10226, 30510, 89665, 260376, 748776, 2136001, 6052062, 17048642 of them from orders two to fifteen. Ideas of dynamical programming for sum of perfect matchings are classical textbook results which can be found in common graph algorithm texts.

Additional complexities are three-fold. There are contact/non-contact switch where parts of them can be reduced by the  $\mathcal{L}$  cover. In addition, one has to remove the disconnected diagrams and switch to momentum space for more compact Monte-Carlo configurations. All of them can be solved in a unified way by just modifying the call graph. We start to propagate through nodes in the original call graph from top to bottom. For the second layer with 1..., each of the nodes now represent a  $\mathcal{L}$  function with one screened interaction and two Green's functions. They have to occupy the same set of Green's functions. As we proceed to the third layer, each nodes, that would contain several sub-graphs, must occupy the same territory (specified by Green's functions it occupies). The territory may contain two  $\mathcal{L}$  functions or one  $\mathcal{L}$  function and another three edges that are not aligned with the  $\mathcal{L}$ -shape topology. Interactions that are not within the  $\mathcal{L}$ -shape topology must be chosen such that it at least connects to two Green's functions within the territory. The way to select territory is always possible when propagating through layers due to our edge connection rules: let  $j$  be the minimum index of the node that is not connected, then the proceeding  $W$  line must connect it and no "skipping" is allowed. With the no "skipping" principle, when selecting territories, one must be able to transverse from one vertex to another within the same territory and within the same cycle without passing any other fermion lines out of the territory and  $W$  lines within or out of the territory. Proving the existence of such territories that satisfy the above three principles is trivial. If there is only one cycle  $(1, \dots, 2n)$ , then one can proceed occupying fermion lines  $(2n, 1)$ ,  $(1, 2)$ ,  $(2, 3)$ ,  $(3, 4)$ , etc. If there are more than one cycles, one proceeds by occupying cycles with smaller indices akin to the one-cycle case.

During this procedure, one needs to add new nodes generated in previous layers. We visualize the procedure below using an example from one screened interaction to two screened interactions. Dark red and green lines label the two territories selected. The node  $\boxed{11010100}$  is formed by  $\boxed{10010000}$  and  $\boxed{10000100}$ .



In the third and fourth diagrams, there are two new nodes generated in the layer above due to the contact interaction contraction. There is no connection between  $\boxed{11000000}$  and  $\boxed{11010100}$ . Otherwise the territory selection rule is violated. Disconnected diagrams can be directly eliminated from the nodes. To relieve the level of abstraction, we give in Appendix. C Fig. 7 a complete call graph at order three.

The above discussions would readily apply to real space with contact/non-contact switch. Momentum assignment can be done on the fly due to the construction of the territory. There is a noticeable case. When there is a screened interaction connecting two different cycles, its momentum is always zero.

## VII. CONCLUSION AND OUTLOOK

We have proposed a promising numerical method based on  $1/N_f$  expansions that is tested for sufficiently large systems with strong interactions at low temperatures for Hubbard-type models. Obvious extensions include changing lattice geometries and interaction types. Generalizing to non-equilibrium that are suited to transport simulations seems feasible but with new problems on optimizing the additional exponential complexity of Keldysh indices summations. To handle the symmetry breaking case, a (conjectured) better way is to expand, not the original  $SU(N_f)$  symmetry but artificially broaden the symmetry to  $SU(N_f) \times SU(M)$ , where certainly the first symmetry may be void [53]. Importantly, to reach high orders for re-summation, we can expand  $W$  rather than  $1/M$ . We notice that quadratic part in  $G$  of Lagrangian could be re-parametrized in a one-parameter family as:

$$(1+a)G_{\alpha\alpha}(i, i; \tau, \tau^+)G_{\beta\beta}(j, j; \tau, \tau^+) + aG_{\beta\alpha}(j, i; \tau, \tau^+)G_{\alpha\beta}(i, j; \tau, \tau^+), \quad (25)$$

where now  $\alpha, \beta$  are spin indices. Topologies of diagrams are identical in two approaches. The additional learnable parameter  $a$  represents mixture between different channels. Since in this paper, we only consider the case of flavour-averaged Green's functions, it is impossible to directly compute order parameters, while it is feasible in the mixed channel. Indeed, symmetry-broken bare U series could also directly compute order parameters but we are in doubt of its convergence for arbitrary band models as explained in the main text. To propose new types of symmetry-broken series beyond the spin-rotation symmetry, semi-bold line series would be the most natural choice out of the dilemma. Old problems such as whether loop current orders can exist in the Hubbard model would require more exotic shifted-expansion point. We left systematic studies of those in the future.

### VIII. ACKNOWLEDGMENTS

B. S. is supported by the Imperial College President's Scholarship. Part of the numerical simulations were performed on the Imperial College HPC cluster. The C++ VEGAS map interface was adapted from [54].

## APPENDIX

### A. More Benchmarks for 2D SU(2) Hubbard Model on the Honeycomb Lattice with Symmetry-Broken Bare U Series

We provide in the appendix more data of shifted bare-U series benchmarked with DQMC simulations.

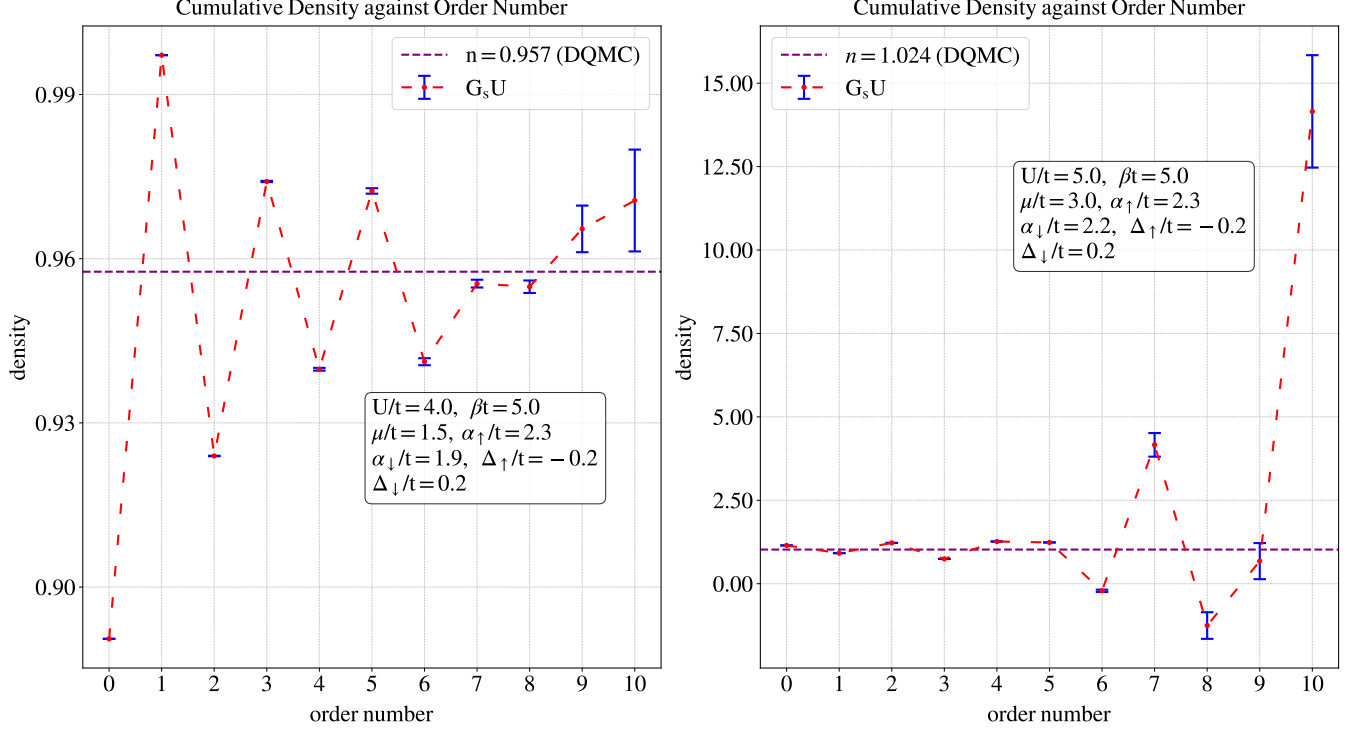


FIG. 5. Cumulative order-by-order density for  $8 \times 8$  honeycomb lattice using shifted bare-U series. Exact value computed DQMC is shown in the legend. Since MC errors at the large expansion orders are large, for LHS plot, we used the first nine orders which gives  $0.9547(3)$  ( $(3, 5)$  Padé). For RHS plot, we used the first eight orders which gives  $1.04(1)$  ( $(2, 5)$  Padé). We discussed two different Padé error propagation. Though the first approach is mathematically rigorous, we found via numerical experiments that the second approach reduces error bars in unbiased way.

As can be seen from the right plot in Fig. 5, series on the right plot diverges while the Padé approximation (discussed later) correctly predict the filling after re-summation. However, we must point out that at many parameters we have tested, different re-summation methods differ significantly. In particular, singularities on the positive real axis under the Borel-Padé approximation that directly leads to failure of re-summation is absent in the Padé approximation. We find the integral approximant method introduced in [50] works poorly in cases with large divergence. The power of re-summation persists to large systems ( $50 \times 50$ ).

We compared two ways of propagating errors in the Padé approximations. Given a list of power series coefficients,  $\bar{a} = \{\bar{a}_i\}$  and its standard deviation  $\{\delta_{\bar{a}_i}\}$ . The first approach to propagate errors is to generate a list of samples following random normal distribution, *i.e.*

$$a_i \sim \exp^{-(a_i - \bar{a}_i)^2 / 2\delta_{\bar{a}_i}^2}. \quad (26)$$

And then the extrapolated error is given by the sample standard deviation of  $\text{Padé}(a)$ . Despite of the conceptual correctness, this approach may overestimate the extrapolated error since some of the generated samples may approach the singularity and significantly proliferate the error bars. In the second approach, we estimate errors using the maximum and minimum values from  $2^{\max \text{ order} + 1}$  samples generated by  $[\bar{a}_0 \pm \delta_{\bar{a}_0}, \bar{a}_1 \pm \delta_{\bar{a}_1}, \dots, \bar{a}_{\max \text{ order}} \pm \delta_{\bar{a}_{\max \text{ order}}}]$ . We found this approach gives much smaller error bars. Certainly, it remains debatable of the correct error propagation procedure. And we leave this issue for future discussions.

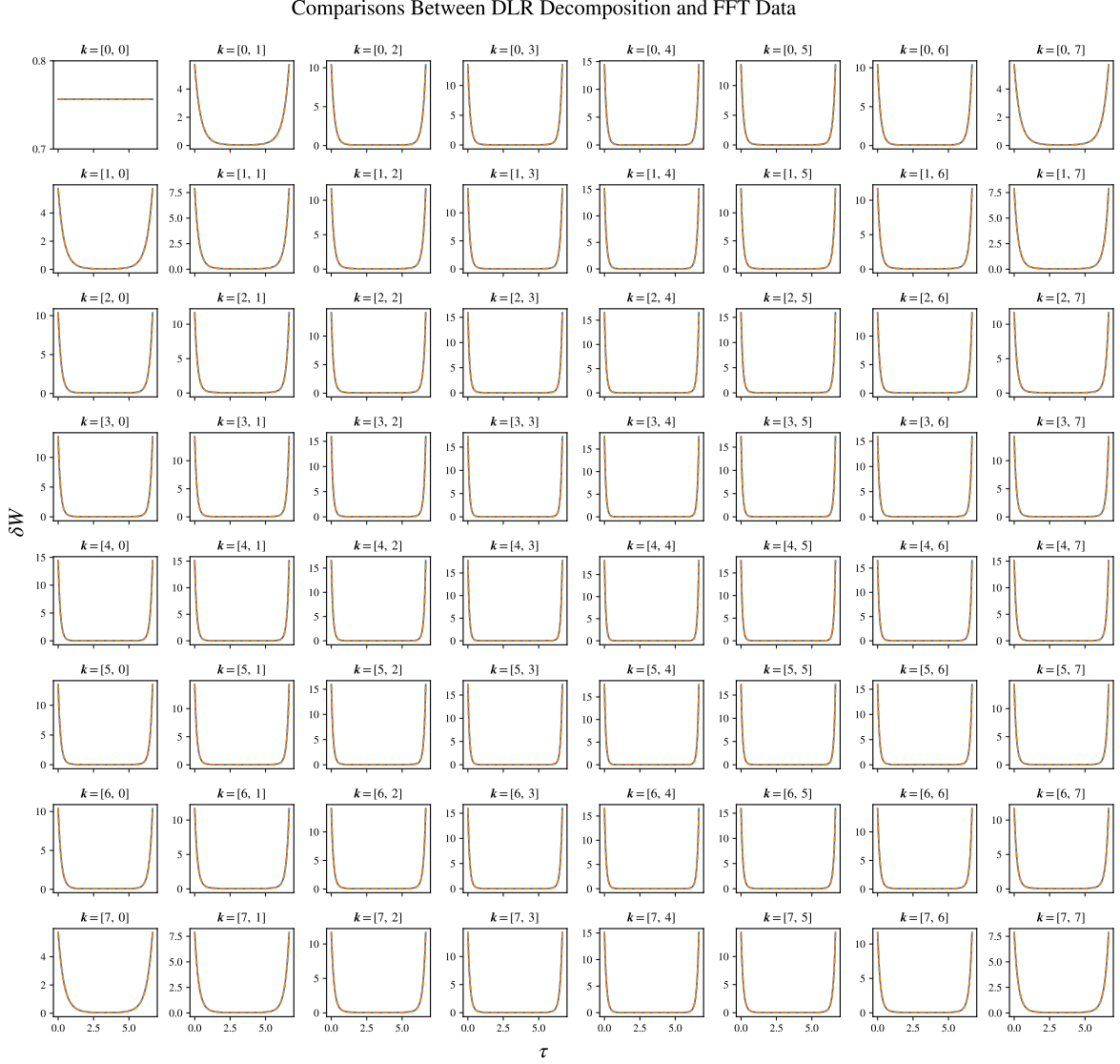


FIG. 6. Comparisons between the data for  $\delta W(\tau, \mathbf{k})$  and its discrete Lehmann representations,  $\delta W(\tau, \mathbf{k}) = \sum_l e^{-\omega_l(\mathbf{k})\tau} \delta W_l(\mathbf{k})$  for 2D  $8 \times 8$  SU(6) Hubbard model on the square lattice at  $U/t = 8$ ,  $\beta t = 6.6667$  and  $\mu/t = 1.746251$ . We choose 10000 points to discretize the uniform mesh in imaginary time and directly solve the integral equation for  $\delta W$ . After preparing the FFT data, we then perform the DLR decomposition with cut-off  $\Lambda = 5\beta$  and  $\epsilon = 10^{-15}$ .

### B. More on Discrete Lehmann Representations

With the DLR data, we then proceed to compute the  $\mathcal{L}$  function (the contact part is trivial and filtered out),

$$\mathcal{L}_{abc}(\tau_1, \tau_2, \mathbf{k}_0, \mathbf{k}_1) = \sum_d \int_{\tau} G_{ad}(\tau_1 - \tau, \mathbf{k}_0) G_{dc}(\tau + \tau_2, \mathbf{k}_1) \delta W_{db}(\tau, \mathbf{k}_0 - \mathbf{k}_1). \quad (27)$$



If  $\tau_1 + \tau_2 < \beta$ , it gives

$$\begin{aligned}
V_{a\alpha} V_{\alpha d}^\dagger V_{d\gamma}' V_{\gamma c}^\dagger & \left\{ \frac{e^{(\beta-\tau_1)\epsilon_\alpha + (\beta-\tau_2)\epsilon_\gamma'}}{(1+e^{\beta\epsilon_\alpha})(1+e^{\beta\epsilon_\gamma'})} \left( \sum_{l \in \mathcal{D}} p_{l,db} \tau_1 + \sum_{l \in \bar{\mathcal{D}}} \frac{p_{l,db}}{\epsilon_\alpha - \epsilon_\gamma' - \omega_{l,db}} \left( e^{\tau_1(\epsilon_\alpha - \epsilon_\gamma' - \omega_{l,db})} - 1 \right) \right) \right. \\
& - \frac{e^{-\tau_1\epsilon_\alpha + (\beta-\tau_2)\epsilon_\gamma'}}{(1+e^{\beta\epsilon_\alpha})(1+e^{\beta\epsilon_\gamma'})} \left( \sum_{l \in \mathcal{D}} p_{l,db} (\beta - \tau_1 - \tau_2) + \sum_{l \in \bar{\mathcal{D}}} \frac{p_{l,db}}{\epsilon_\alpha - \epsilon_\gamma' - \omega_{l,db}} \left( e^{(\beta-\tau_2)(\epsilon_\alpha - \epsilon_\gamma' - \omega_{l,db})} - e^{\tau_1(\epsilon_\alpha - \epsilon_\gamma' - \omega_{l,db})} \right) \right) \\
& \left. + \frac{e^{-\tau_1\epsilon_\alpha + (2\beta-\tau_2)\epsilon_\gamma'}}{(1+e^{\beta\epsilon_\alpha})(1+e^{\beta\epsilon_\gamma'})} \left( \sum_{l \in \mathcal{D}} p_{l,db} \tau_2 + \sum_{l \in \bar{\mathcal{D}}} \frac{p_{l,db}}{\epsilon_\alpha - \epsilon_\gamma' - \omega_{l,db}} \left( e^{\beta(\epsilon_\alpha - \epsilon_\gamma' - \omega_{l,db})} - e^{(\beta-\tau_2)(\epsilon_\alpha - \epsilon_\gamma' - \omega_{l,db})} \right) \right) \right\}
\end{aligned} \tag{28}$$

If  $\tau_1 + \tau_2 > \beta$ , it gives

$$\begin{aligned}
V_{a\alpha} V_{\alpha d}^\dagger V_{d\gamma}' V_{\gamma c}^\dagger & \left\{ \frac{e^{(\beta-\tau_1)\epsilon_\alpha + (\beta-\tau_2)\epsilon_\gamma'}}{(1+e^{\beta\epsilon_\alpha})(1+e^{\beta\epsilon_\gamma'})} \left( \sum_{l \in \mathcal{D}} p_{l,db} (\beta - \tau_2) + \sum_{l \in \bar{\mathcal{D}}} \frac{p_{l,db}}{\epsilon_\alpha - \epsilon_\gamma' - \omega_{l,db}} \left( e^{(\beta-\tau_2)(\epsilon_\alpha - \epsilon_\gamma' - \omega_{l,db})} - 1 \right) \right) \right. \\
& - \frac{e^{(\beta-\tau_1)\epsilon_\alpha + (2\beta-\tau_2)\epsilon_\gamma'}}{(1+e^{\beta\epsilon_\alpha})(1+e^{\beta\epsilon_\gamma'})} \left( \sum_{l \in \mathcal{D}} p_{l,db} (\tau_1 + \tau_2 - \beta) + \sum_{l \in \bar{\mathcal{D}}} \frac{p_{l,db}}{\epsilon_\alpha - \epsilon_\gamma' - \omega_{l,db}} \left( e^{\tau_1(\epsilon_\alpha - \epsilon_\gamma' - \omega_{l,db})} - e^{(\beta-\tau_2)(\epsilon_\alpha - \epsilon_\gamma' - \omega_{l,db})} \right) \right) \\
& \left. + \frac{e^{-\tau_1\epsilon_\alpha + (2\beta-\tau_2)\epsilon_\gamma'}}{(1+e^{\beta\epsilon_\alpha})(1+e^{\beta\epsilon_\gamma'})} \left( \sum_{l \in \mathcal{D}} p_{l,db} (\beta - \tau_1) + \sum_{l \in \bar{\mathcal{D}}} \frac{p_{l,db}}{\epsilon_\alpha - \epsilon_\gamma' - \omega_{l,db}} \left( e^{\beta(\epsilon_\alpha - \epsilon_\gamma' - \omega_{l,db})} - e^{\tau_1(\epsilon_\alpha - \epsilon_\gamma' - \omega_{l,db})} \right) \right) \right\},
\end{aligned} \tag{29}$$

where  $V$  and  $V^\dagger$  are unitary matrices diagonalizing the momentum space free Green's function,  $p$  and  $\omega$  follow from conventions in the main text. To simplify notations,  $V$  and  $\epsilon$  symbols with  $\prime$  are for  $\mathbf{k}_1$ ;  $V$  and  $\epsilon$  symbols without  $\prime$  are for  $\mathbf{k}_0$ .  $\mathcal{D}$  and  $\bar{\mathcal{D}}$  denotes resonant and non-resonant sets of  $l$  when  $\epsilon - \epsilon' - \omega = 0$  or  $\neq 0$ . To handle the summation of large exponentials, it would be better to re-organize terms in terms of product of fermi functions

$$f_F(\tau) = -e^{-\tau\epsilon}/(1+e^{\beta\epsilon}) \text{ if } \tau \leq 0 \quad , \quad f_F(\tau) = e^{(\beta-\tau)\epsilon}/(1+e^{\beta\epsilon}) \text{ if } \tau > 0. \tag{30}$$

If the temperature is low enough such that  $\omega$ 's and  $p$ 's are large (typically with large cut-off  $\Lambda$  and low tolerance  $\epsilon$ ), we switch to **long double** for summations of the type

$$\sum_l \frac{pl}{\epsilon - \epsilon' - \omega_l} e^{-\omega_l \tau}. \tag{31}$$

### C. Modified Call Graph

The modified call graph at order 3 with partition (6,) is given explicitly in Fig. 7. The first and last layers are trivial and not added.

### D. List of Parameters for MCMC

We give the full list of parameters and their typical values used for controlling the accuracy of the simulation. We choose a uniform mesh in the imaginary time  $[\epsilon, \beta - \epsilon]$ , where a small  $\tau$ -grid shift  $\epsilon$  is to avoid discontinuities at the boundaries. We introduced an auxiliary  $x$  variable to compute  $\ln Z_{\text{RPA}}$  and numerical integration over  $x$  are performed using trapezoidal rule with  $N_x$  points in  $[0, 1]$ . For the discrete Lehman representation, we reduce the error by tuning tolerance ( $\text{DLR}_{\text{tol}}$ ) and cut-off ( $\text{DLR}_\Lambda$ ). We use central differentiation to compute density and energy

$$n = \frac{\ln Z(\mu + h_\mu) - \ln Z(\mu - h_\mu)}{2N h_\mu}, \quad E = -\frac{\ln Z(\beta + h_\beta) - \ln Z(\beta - h_\beta)}{2N h_\beta} + \mu \frac{\ln Z(\mu + h_\mu) - \ln Z(\mu - h_\mu)}{2N h_\mu}. \tag{32}$$

To avoid MC error bar proliferation, we found it is advantageous to directly perform the numerical differentiation within the integrand. For VEGAS map, we also introduce a damping factor  $\alpha_\alpha$  for the original VEGAS damping  $\alpha$  during map iterations to gradually reduce  $\alpha$ , where we found too high  $\alpha$  values could lead to degenerate grids and could not stabilize the map.

Param	Symbol	Typical Value
Number of $\tau$ grid points	$N_{\text{UM}}$	5000
$\tau$ grid shifts	$\epsilon$	$10^{-14}$
Number of $x$ grid points	$N_x$	30
DLR tol	$\text{DLR}_{\text{tol}}$	$10^{-15}$
DLR $\Lambda$	$\text{DLR}_{\Lambda}$	$5\beta$
Chemical Potential Shift	$h_{\mu}$	0.01
Inverse Temperature Shift	$h_{\beta}$	0.02
MCMC Warm-up Periods	$N_{\text{warm}}$	$2^{17}$
MCMC Updates	$N_{\text{MC}}$	$2^{30}$
VEGAS training per iteration	$N_{\text{VEGAS}}$	$2^{17}$
Number of VEGAS iterations	$N_{\text{iter}}$	64
Number of MC Samplings for $\mathcal{N}$	$N_{\mathcal{N}}$	$2^{26}$
Number of VEGAS Intervals	$N_I$	100
VEGAS Damping $\alpha$	$\alpha$	0.8
$\alpha$ for VEGAS Damping $\alpha$	$\alpha_{\alpha}$	1.1
Number of MCMC Chains	$N_{\text{chains}}$	500

TABLE IV. List of parameters to control the simulation accuracy.

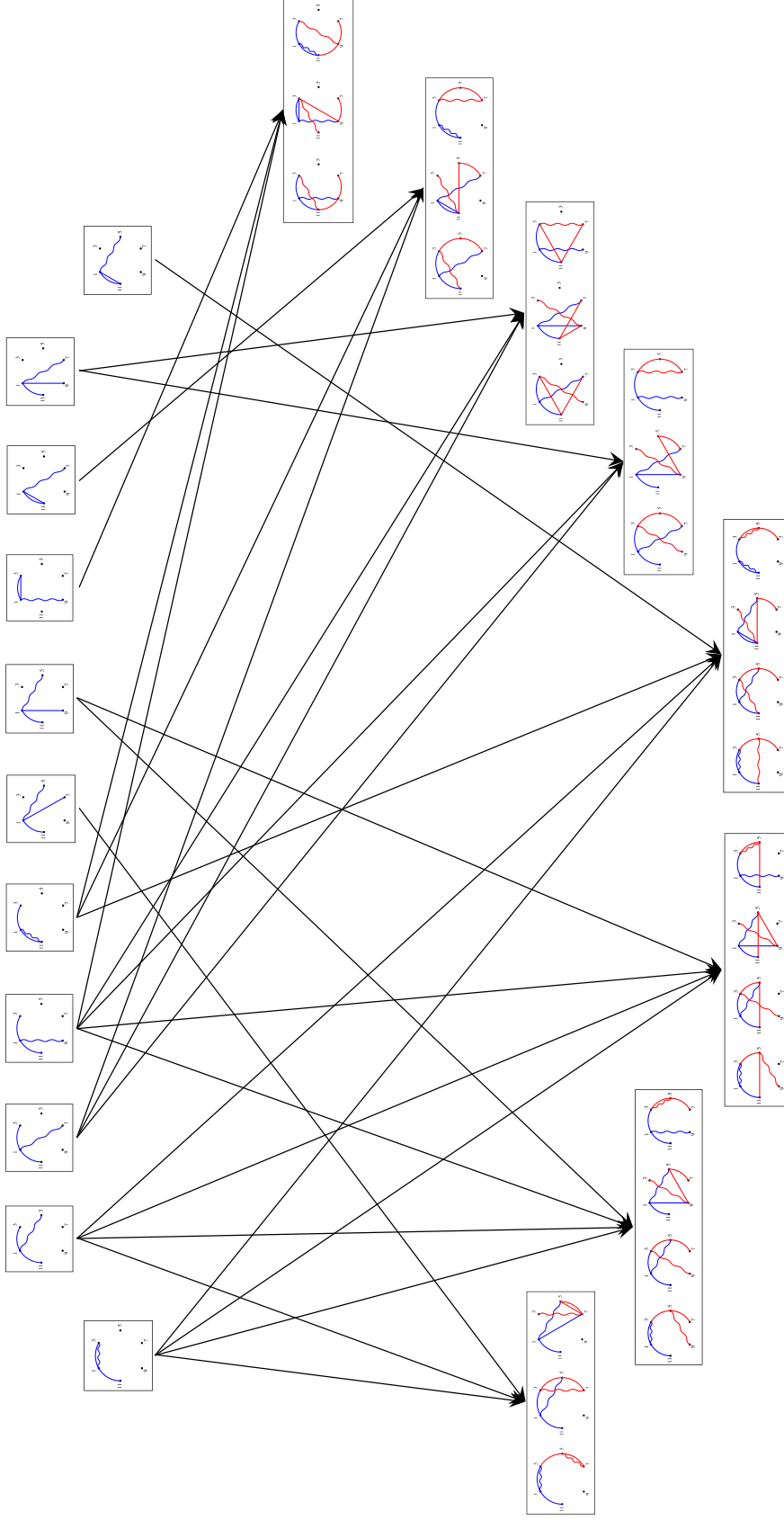


FIG. 7. The modified call graph at order 3 with partition (6, ) following the rules outlined in the main texts. Territories are colored by blue and red. Nodes are labeled as 1, 3, 5, 7, 9, 11. Each edge connecting two different layers consists of three parts, two Green's functions and one interaction. While if an interaction has an end hanging, it is a bare interaction. Momentum can be assigned based on this that should maximize the re-usability. The topmost and bottommost layers with all 0's and all 1's are not shown. The first five boxes on the first layer are from the original call graph while the contact interaction contractions generate another six boxes. There are two boxes on the second layer that are generated when connecting to the bottommost layer, where each of the original six boxes now contain new graphs generated by contact interaction contractions.

- 
- [1] F. Aryasetiawan and O. Gunnarsson, The gw method, *Reports on Progress in Physics* **61**, 237 (1998).
- [2] A. Georges, G. Kotliar, W. Krauth, and M. J. Rozenberg, Dynamical mean-field theory of strongly correlated fermion systems and the limit of infinite dimensions, *Rev. Mod. Phys.* **68**, 13 (1996).
- [3] U. Schollwöck, The density-matrix renormalization group, *Rev. Mod. Phys.* **77**, 259 (2005).
- [4] J. I. Cirac, D. Pérez-García, N. Schuch, and F. Verstraete, Matrix product states and projected entangled pair states: Concepts, symmetries, theorems, *Rev. Mod. Phys.* **93**, 045003 (2021).
- [5] W. Metzner, M. Salmhofer, C. Honerkamp, V. Meden, and K. Schönhammer, Functional renormalization group approach to correlated fermion systems, *Rev. Mod. Phys.* **84**, 299 (2012).
- [6] Z.-X. Li and H. Yao, Sign-problem-free fermionic quantum monte carlo: Developments and applications, *Annual Review of Condensed Matter Physics* **10**, 337 (2019).
- [7] J. E. Hirsch, Two-dimensional hubbard model: Numerical simulation study, *Phys. Rev. B* **31**, 4403 (1985).
- [8] S. R. White, D. J. Scalapino, R. L. Sugar, E. Y. Loh, J. E. Gubernatis, and R. T. Scalettar, Numerical study of the two-dimensional hubbard model, *Phys. Rev. B* **40**, 506 (1989).
- [9] M. Rigol, T. Bryant, and R. R. P. Singh, Numerical linked-cluster approach to quantum lattice models, *Phys. Rev. Lett.* **97**, 187202 (2006).
- [10] R. O. Jones, Density functional theory: Its origins, rise to prominence, and future, *Rev. Mod. Phys.* **87**, 897 (2015).
- [11] J. Sturt and E. Kozik, Exploiting parallelism for fast feynman diagrammatics, arXiv preprint arXiv:2501.00675 (2025).
- [12] S. A. Kulagin, N. Prokof'ev, O. A. Starykh, B. Svistunov, and C. N. Varney, Bold diagrammatic monte carlo method applied to fermionized frustrated spins, *Phys. Rev. Lett.* **110**, 070601 (2013).
- [13] K. Van Houcke, F. Werner, T. Ohgoe, N. V. Prokof'ev, and B. V. Svistunov, Diagrammatic monte carlo algorithm for the resonant fermi gas, *Phys. Rev. B* **99**, 035140 (2019).
- [14] R. Rossi, F. Werner, N. Prokof'ev, and B. Svistunov, Shifted-action expansion and applicability of dressed diagrammatic schemes, *Phys. Rev. B* **93**, 161102(R) (2016).
- [15] F. Šimkovic IV, R. Rossi, and M. Ferrero, Efficient one-loop-renormalized vertex expansions with connected determinant diagrammatic monte carlo, *Phys. Rev. B* **102**, 195122 (2020).
- [16] E. Kozik, Combinatorial summation of feynman diagrams: Equation of state of the 2d su(n) hubbard model, *Nat. Commun.* **15**, 7916 (2024).
- [17] S. Taie, E. Ibarra-García-Padilla, N. Nishizawa, Y. Takasu, Y. Kuno, H.-T. Wei, R. T. Scalettar, K. R. A. Hazzard, and Y. Takahashi, Observation of antiferromagnetic correlations in an ultracold su(n) hubbard model, *Nat. Phys.* **18**, 1356 (2022).
- [18] G. Pasqualetti, O. Bettermann, N. Darkwah Oppong, E. Ibarra-García-Padilla, S. Dasgupta, R. T. Scalettar, K. R. A. Hazzard, I. Bloch, and S. Fölling, Equation of state and thermometry of the 2d SU(n) fermi-hubbard model, *Phys. Rev. Lett.* **132**, 083401 (2024).
- [19] K. Van Houcke, E. Kozik, N. Prokof'ev, and B. Svistunov, Diagrammatic monte carlo, *Physics Procedia* **6**, 95 (2010), computer Simulations Studies in Condensed Matter Physics XXI.
- [20] E. Bourovski, N. Prokof'ev, and B. Svistunov, Truncated-determinant diagrammatic monte carlo for fermions with contact interaction, *Phys. Rev. B* **70**, 193101 (2004).
- [21] A. N. Rubtsov, V. V. Savkin, and A. I. Lichtenstein, Continuous-time quantum monte carlo method for fermions, *Phys. Rev. B* **72**, 035122 (2005).
- [22] E. Burovski, N. Prokof'ev, B. Svistunov, and M. Troyer, Critical temperature and thermodynamics of attractive fermions at unitarity, *Phys. Rev. Lett.* **96**, 160402 (2006).
- [23] R. Rossi, Determinant diagrammatic monte carlo algorithm in the thermodynamic limit, *Phys. Rev. Lett.* **119**, 045701 (2017).
- [24] Y. Núñez Fernández, M. Jeannin, P. T. Dumitrescu, T. Kloss, J. Kaye, O. Parcollet, and X. Waintal, Learning feynman diagrams with tensor trains, *Phys. Rev. X* **12**, 041018 (2022).
- [25] F. Šimkovic IV and M. Ferrero, Fast principal minor algorithms for diagrammatic monte carlo, *Phys. Rev. B* **105**, 125104 (2022).
- [26] K. Chen and K. Haule, A combined variational and diagrammatic quantum monte carlo approach to the many-electron problem, *Nat. Commun.* **10**, 3725 (2019).
- [27] H. Flyvbjerg and H. G. Petersen, Error estimates on averages of correlated data, *J. Chem. Phys.* **91**, 1113 (1989).
- [28] S. Kirkpatrick, C. D. Gelatt, and M. P. Vecchi, Optimization by simulated annealing, *Science* **220**, 671 (1983).
- [29] G. Peter Lepage, A new algorithm for adaptive multidimensional integration, *Journal of Computational Physics* **27**, 192 (1978).
- [30] G. P. Lepage, Adaptive multidimensional integration: vegas enhanced, *Journal of Computational Physics* **439**, 110386 (2021).
- [31] C. P. Robert and G. Casella, *Monte Carlo Statistical Methods*, 2nd ed., Springer Texts in Statistics (Springer, New York, NY, 2004).
- [32] L. Martino, D. Luengo, and J. Míguez, *Independent Random Sampling Methods*, 1st ed., Statistics and Computing (Springer, Cham, 2018).
- [33] A. Gelman and D. B. Rubin, Inference from Iterative Simulation Using Multiple Sequences, *Statistical Science* **7**, 457 (1992).

- [34] Y. Deng, E. Kozik, N. V. Prokof'ev, and B. V. Svistunov, Emergent bcs regime of the two-dimensional fermionic hubbard model: Ground-state phase diagram, *EPL* **110**, 57001 (2015).
- [35] A. Kitaev and S. J. Suh, The soft mode in the sachdev-ye-kitaev model and its gravity dual, *JHEP* **2018**, 183.
- [36] I. Esterlis, H. Guo, A. A. Patel, and S. Sachdev, Large- $n$  theory of critical fermi surfaces, *Phys. Rev. B* **103**, 235129 (2021).
- [37] The convention is  $Z = \int \mathcal{D}\Sigma \mathcal{D}G e^{-S}$ , where  $Z$  is the grand-canonical partition function.
- [38] With the momentum and internal band indices hidden and internal matrix multiplication is implicitly indicated. We choose the Fourier transform convention as

$$\mathbf{c}_{\mathbf{k}} = \frac{1}{\sqrt{N_1 N_2}} \sum_{\mathbf{R}_i} \mathbf{c}_{\mathbf{R}_i} e^{i\mathbf{k} \cdot \mathbf{R}_i},$$

i.e. no internal phase factor between two sites in a unit cell.

- [39] L. Cordella, P. Foggia, C. Sansone, and M. Vento, A (sub)graph isomorphism algorithm for matching large graphs, *IEEE Transactions on Pattern Analysis and Machine Intelligence* **26**, 1367 (2004).
- [40] L. P. Cordella, P. Foggia, C. Sansone, and M. Vento, An improved algorithm for matching large graphs, in *3rd IAPR-TC15 Workshop on Graph-based Representations in Pattern Recognition* (Cuen, 2001) pp. 149–159.
- [41] A. Hagberg, D. Schult, and P. Swart, Networkx: Network analysis in python, <https://github.com/networkx> (2004-2024).
- [42] R. Rossi, N. Prokof'ev, B. Svistunov, K. V. Houcke, and F. Werner, Polynomial complexity despite the fermionic sign, *EPL* **118**, 10004 (2017).
- [43] J. Kaye, K. Chen, and O. Parcollet, Discrete lehmann representation of imaginary time green's functions, *Phys. Rev. B* **105**, 235115 (2022).
- [44] J. Kaye, K. Chen, and H. U. Strand, libldr: Efficient imaginary time calculations using the discrete lehmann representation, *Computer Physics Communications* **280**, 108458 (2022).
- [45] S.-S. Lee, Low-energy effective theory of fermi surface coupled with u(1) gauge field in 2 + 1 dimensions, *Phys. Rev. B* **80**, 165102 (2009).
- [46] F. Šimkovic IV, J. P. F. LeBlanc, A. J. Kim, Y. Deng, N. V. Prokof'ev, B. V. Svistunov, and E. Kozik, Extended crossover from a fermi liquid to a quasiantiferromagnet in the half-filled 2d hubbard model, *Phys. Rev. Lett.* **124**, 017003 (2020).
- [47] P. Weinberg and M. Bukov, QuSpin: a Python package for dynamics and exact diagonalisation of quantum many body systems part I: spin chains, *SciPost Phys.* **2**, 003 (2017).
- [48] P. Weinberg and M. Bukov, QuSpin: a Python package for dynamics and exact diagonalisation of quantum many body systems. Part II: bosons, fermions and higher spins, *SciPost Phys.* **7**, 020 (2019).
- [49] J. P. F. LeBlanc, A. E. Antipov, F. Becca, I. W. Bulik, G. K.-L. Chan, C.-M. Chung, Y. Deng, M. Ferrero, T. M. Henderson, C. A. Jiménez-Hoyos, E. Kozik, X.-W. Liu, A. J. Millis, N. V. Prokof'ev, M. Qin, G. E. Scuseria, H. Shi, B. V. Svistunov, L. F. Tocchio, I. S. Tupitsyn, S. R. White, S. Zhang, B.-X. Zheng, Z. Zhu, and E. Gull (Simons Collaboration on the Many-Electron Problem), Solutions of the two-dimensional hubbard model: Benchmarks and results from a wide range of numerical algorithms, *Phys. Rev. X* **5**, 041041 (2015).
- [50] F. Šimkovic and E. Kozik, Determinant monte carlo for irreducible feynman diagrams in the strongly correlated regime, *Phys. Rev. B* **100**, 121102 (2019).
- [51] R. Garioud, F. Šimkovic, R. Rossi, G. Spada, T. Schäfer, F. Werner, and M. Ferrero, Symmetry-broken perturbation theory to large orders in antiferromagnetic phases, *Phys. Rev. Lett.* **132**, 246505 (2024).
- [52] B. Cohen-Stead, S. M. Costa, J. Neuhaus, A. T. Ly, Y. Zhang, R. Scalettar, K. Barros, and S. Johnston, SmoQyDQMC.jl: A flexible implementation of determinant quantum Monte Carlo for Hubbard and electron-phonon interactions, *SciPost Phys. Codebases*, 29 (2024).
- [53] D. P. Arovas, E. Berg, S. A. Kivelson, and S. Raghu, The hubbard model, *Annual Review of Condensed Matter Physics* **13**, 239 (2022).
- [54] Y. Wu, Cigar: C++ implementation of vegas/vegas+ algorithm (cigar) for multi-dimension integral., <https://github.com/ycwu1030/CIGAR> (2020).